Real-time tracking of vesicles in living cells reveals that tau-hyperphosphorylation suppresses unidirectional transport by motor proteins

Eunsang Lee[a, 1], Donghee Kim[b,c,d, 1], Yo Han Song[a, 1], Kyujin Shin[e], Sanggeun Song[b,c,d], Minho Lee[b,c,d], Yeongchang Goh[a], Mi Hee Lim[f], Ji-Hyun Kim[b,c], Jaeyoung Sung[b,c,d,*] and Kang Taek Lee[a,*]

Affiliations:

[a]Department of Chemistry, School of Physics and Chemistry, Gwangju Institute of Science and Technology (GIST), Gwangju 61005, Republic of Korea

[b]Creative Research Initiative Center for Chemical Dynamics in Living Cells, Chung-Ang University, Seoul 06974, Republic of Korea

[c]Department of Chemistry, Chung-Ang University, Seoul 06974, Republic of Korea

[d]National Institute of Innovative Functional Imaging, Chung-Ang University, Seoul 06974, Republic of Korea

[e]Materials Research & Engineering Center (MREC), R&D Division, Hyundai Motor Company, Uiwang 16082, Republic of Korea

[f]Department of Chemistry, Korea Advanced Institute of Science and Technology (KAIST), Daejeon 34141, Republic of Korea

* Jaeyoung Sung and Kang Taek Lee

Email: jaeyoung@cau.ac.kr and ktlee@gist.ac.kr

Author Contributions: [1] E.L., D.K., and Y.H.S. contributed equally to this work.

Keywords: motor protein, microtubule, transport dynamics, tau aggregation, upconverting nanoparticle

Abstract

Synaptic vesicle transport by motor proteins along microtubules is a crucial active process underlying neuronal communication. It is known that microtubules are destabilized by tau-hyperphosphorylation, which causes tau proteins to detach from microtubules and form neurofibril tangles. However, how tau-phosphorylation affects transport dynamics of motor proteins on the microtubule remains unknown. Here, we discover that long-distance unidirectional motion of vesicle-motor protein multiplexes (VMPMs) in living cells is suppressed under tau-hyperphosphorylation, with the consequent loss of fast vesicle-transport along the microtubule. The VMPMs in hyperphosphorylated cells exhibit seemingly bidirectional random motion, with dynamic properties far different from VMPM motion in normal cells. We establish a parsimonious physicochemical model of VMPM's active motion that provides a unified, quantitative explanation and predictions for our experimental results. Our analysis reveals that, under hyperphosphorylation conditions, motor-protein-multiplexes have both static and dynamic motility fluctuations. The loss of the fast vesicle-transport along the microtubule can be a mechanism of neurodegenerative disorders associated with tau-hyperphosphorylation.

INTRODUCTION

Neuronal communication is achieved by active transport of synaptic vesicles by kinesins and dyneins.[1-7] These molecular motors catalyze ATP-hydrolysis and convert the resulting chemical energy to mechanical energy required for their motion along the microtubule, a eukaryotic cytoskeleton formed by the polymerization of tubulin proteins. In the microtubule, tubulins are cross-linked by tau proteins to yield a stable helical structure, which produces the polarity of the microtubule.[8-10] This polarity allows kinesins and dyneins to move in the opposite direction from each other along the microtubule. Thus, a stable helical structure of the microtubule is essential for the microtubule-based directional motion of these motor proteins, which underlies many important biological processes, including the self-assembly and positioning of the mitotic spindle in cell division and the transport of various subcellular cargos ranging from vesicles to mitochondria.[11-14]

Vesicles carried by these motor proteins exhibit unique transport dynamics far different from the dynamics of simple active matter motion or any kind of passive thermal motion. In living cells, multiple kinesins and dyneins are bound to a single vesicle and transport it along the microtubule.[15, 16] In normal neuronal cells, this vesicle-motor protein multiplex (VMPM) exhibits multimode transport dynamics.[17] When the force on the vesicle exerted by kinesins in the anterograde direction (the direction towards the cell membrane) is in a delicate balance with the force exerted by dyneins in the retrograde direction (the direction towards the nucleus), the VMPM displays seemingly random bidirectional motion, as modeled by a tug-of-war.[18-22] The VMPM also shows unidirectional motion when either kinesin or dynein motors exert a far greater force on the vesicle [23, 24], although the unidirectional motion of the VMPM is less frequent than the bidirectional

motion.[17] At short times, fast liberation of the vesicle tethered to the motor protein multiplex (MPM) is dominant compared to the MPM motion along the microtubule. The resulting motion of the VMPM exhibits short-time sub-diffusion, transitioning to intermediate super-diffusion, and then ultimate diffusive motion.[17, 25] This multimode transport dynamics of the VMPM in living cells was quantitatively explained by considering the reversible switching between unidirectional and bidirectional modes of the MPM as well as the liberational motion of the vesicle.[17, 26]

In cells under hyperphosphorylation conditions, the motion of VMPMs along the microtubule is expected to differ from their motion in normal cells. Hyperphosphorylated tau has been identified in many neurodegenerative diseases, including Alzheimer's disease, Down syndrome, and CBD.[27] In particular, the concentration of hyperphosphorylated tau proteins in the brains of Alzheimer's disease patients is found to be 3 to 4 times higher than that in normal adult brains.[28, 29] Tau is a microtubule associated protein that plays a central role in nerve cells by maintaining cytoskeleton stability, regulating microtubule dynamics, promoting axon growth, and regulating axon migration.[30, 31] Abnormally hyperphosphorylated tau proteins aggregate to form insoluble paired helical filaments (PHFs) and higher-order structures called intracellular neurofibrillary tangles (NFTs).[32-35] NFTs are a primary marker of neurodegenerative disorders, such as Alzheimer's and Parkinson's; however, it is a controversial issue whether NFTs are their primary cause.[36, 37] When hyperphosphorylated tau loses its affinity for microtubules and aggregates with tau oligomers in the cytoplasm, its ability to promote microtubule assembly or bind to microtubules is lost, resulting in the collapse of microtubules [32, 38-43].

Despite extensive studies on the hyperphosphorylation of tau and the NFT formation and its physiological consequences,[32, 44] we do not yet know how tau-phosphorylation and ensuing tau-

detachment from the microtubule affect the vesicle delivery dynamics of the VMPM along the microtubule. Tau in the microtubule can inhibit kinesin motion. A recent *in vitro* study showed that the speed of kinesin motion along the microtubule decreases with the concentration of tau in the microtubule.[3, 45-50] This does not necessarily mean, however, that the VMPMs move faster upon hyperphosphorylation-induced tau detachment from the microtubule. So far, there is no quantitative understanding about the effects of tau-hyperphosphorylation on the VMPM motion along the microtubule.

To shed light on this issue, we monitored and analyzed individual trajectories of VMPMs along tau-deficient microtubules in living cells under hyperphosphorylation conditions. We treated human neuroblastoma cells with Forskolin, which results in a hyperphosphorylation-induced tau detachment from the microtubule.[51] Using upconverting nanoparticle (UCNP) probes free of photobleaching or photoblinking, we tracked nearly 450 individual trajectories of VMPMs in our cell system. Our investigation showed that, upon tau-hyperphosphorylation, unidirectional motion of the MPM is suppressed and the MPM effectively exhibits stochastic motion which appears Fickian-yet non-Gaussian diffusion along the microtubule in our experimental time resolution, 0.1 seconds. The observed transport dynamics of the VMPM is found to have qualitatively different stochastic properties from the previously reported thermal motion or active motion[52-54]. We propose a parsimonious physicochemical model of VMPM's active motion in hyperphosphorylated cells and performed a quantitative analysis of our experimentally monitored VMPM motion using the model. This simple model is found to provide a simultaneous explanation of the mean square displacement and the non-Gaussian parameter of the VMPM displacement distribution (VDD) and accurate predictions for the VDD in hyperphosphorylated cells at various

time points. Our analysis shows the presence of both static and dynamic heterogeneity in motility of the MPMs in the forskolin-treated cells. The loss of fast synaptic vesicle transport along the microtubule upon tau-hyperphosphorylation can be a functional mechanism underlying diverse neurodegenerative disorders associated with tau-hyperphosphorylation [27].

RESULT

System and Probe

Real-time trajectories of about 450 individual endosomal vesicles in a neuronal phenotype of human neuroblastoma SH-SY5Y cells under hyperphosphorylation conditions were collected (see Figure 1 and Supplementary video for the real-time video of a few UCNP containing vesicles moving along the axonal microtubule). To induce the hyperphosphorylation conditions, we treated our cells with 20μM of forskolin for 24 hours (see Material and Methods). It was previously reported that Forskolin is not cytotoxic when its concentration is less than 20 μM.[51, 55, 56] Thus, we treat our cells with 20 μM Forskolin to induce hyperphosphorylation of tau proteins. Hyperphosphorylation of tau protein in our cell system was confirmed by Western blotting. (Figures 1b and S2). As an imaging probe, we employed the upconverting nanoparticle (UCNP), free of photobleaching or photoblinking (see Material and Methods and Figures S1 and S3), which enables accurate, long-time tracking of vesicle motion in living cells.[57] The conventional fluorescence probes have many important applications in the field of high-resolution microscopy and single molecule experiments.[57-63] However, for single vesicle tracking in living cells, our UCNP is advantageous over conventional fluorescence probes because of its outstanding photostability and low toxicity.[64]

Primary direction of VMPM motion in hyperphosphorylated cells

The VMPMs motion along the microtubule is far more pronounced than the motion in the microtubule-orthogonal direction in forskolin-treated cells as well as in normal cells[17] (Figure S4). This indicates that, even in our forskolin-treated cells, the microtubules are not broken apart and still play important roles in the microtubule-based transport of vesicles by motor proteins. We focused on VMPM motion in the microtubule direction in this work, unless stated otherwise.

No preferred direction in VMPM motion along the microtubule

VMPM motion does not exhibit any bias between anterograde and retrograde directions along the microtubule. Individual VMPMs show stochastic motion biased in either the anterograde or retrograde direction; however, the mean displacement averaged over VMPMs is not biased to either of these two directions (see the inset shown in Figure 1d). This is also the case for normal cells [17]. Likewise, VMPM motion in the microtubule-orthogonal direction does not show any bias between upward and downward directions (see the inset presented in Figure 1e).

Unique stochastic properties of VMPM motion in hyperphosphorylated cells

The mean squared displacement (MSD) of VMPMs exhibits transient super-diffusive dynamics in normal cells, resulting from unidirectional MPM motion. In the forskolin-treated cells, however, the MSD does not exhibit such transient super-diffusive dynamics (Figure 2a). This observation indicates that, upon tau-hyperphosphorylation, unidirectional motion of MPM is suppressed.

Although active motion of the VMPMs appears bidirectional random motion in forskolin-treated cells, in stark contrast to active matter usually exhibiting unidirectional motion, their

motion here has stochastic properties far different from thermal motion of molecules in complex fluids[65] or the Fickian yet non-Gaussian diffusion of colloidal beads along lipid tubes.[66] One of the most prominent features is that the long-time saturation of the non-Gaussian parameter (NGP) of the vesicle displacement to a constant value at our experimental time scale (Figure 2b). This is in contrast with the NGP time-profiles of molecules and colloids undergoing thermal motion in complex fluidic systems, which asymptotically decreases with time t following t^{-1} at long times.[65]

The NGP, $\alpha_{2,x}(t)$, is defined by $\alpha_{2,x}(t) \equiv \langle d_x^4 \rangle / (3\langle d_x^2 \rangle^2) - 1$ where $\left\langle d_x^n \right\rangle$ denotes the nth moment of the vesicle displacement, d_x (see also Materials and Methods). When the displacement distribution is Gaussian, the NGP vanishes; however, when the displacement distribution deviates from Gaussian, the NGP assumes a finite value. A NGP carries information about the heterogeneity of the vesicle motility and its time-dependent relaxation. The long-time saturation of the NGP value signifies the presence of static heterogeneity in VMPM motility or dynamic heterogeneity of VMPM motility whose relaxation time scale is longer than our observation time scale. The experimentally measured time-profiles of the MSD and NGP of VMPM motion in forskolin-treated cells cannot be explained by previously reported models.

Model and Theory of VMPM motion

To explain the MSD and NGP time-profiles of the observed VMPM motion, we should account for both VMPM motion along the microtubule and the liberational motion of a vesicle bound to the MPM. For this model, the displacement, d_x,of a vesicle can be represented by $d_x = R_x + x'$, where R_x and x' denote, respectively, the displacement of motor protein

multiplex (MPM) and the change in the relative position of the vesicle with respect to the MPM. We assume that vesicle's librational motion around the MPM is so fast that x' assumes a stationary distribution in our experimental time scale. Our experimental results shown in Figure 2 tell us that the MPM motion in our forskolin-treated cells is non-Gaussian diffusion, which emerges when the motility of the MPM is distributed.[65-74]

To explain our experiment, we construct a physicochemical model of the MPM motion in our system, in which MPMs alternatingly undergo unidirectional active motion and random changes in the direction of active motion. In this model, we assume that the MPM's motility is dependent on the state, Γ, of the MPM and the microtubule.[65] Using this model, we obtain the following analytic expressions of the MSD and NGP, $\langle d_x^2(t)\rangle$ and $\alpha_{2,x}(t)\left[\equiv \langle d_x^4\rangle / \left(3\langle d_x^2\rangle^2\right) - 1\right]$, of the VMPM displacement at time scales longer than the time scale of random changes in the direction of MPM's active motion (see Material and Methods)

$$\langle d_x^2(t)\rangle = 2\langle D_\Gamma\rangle t + \langle x'^2\rangle \tag{1a}$$

$$\alpha_{2,x}(t) = \frac{8}{\langle d_x^2(t)\rangle^2}\int_0^t dt'(t-t')\langle \delta D_\Gamma(t')\delta D_\Gamma(0)\rangle + \frac{\langle x'^2\rangle^2}{\langle d_x^2(t)\rangle^2}\alpha_2\left(x'\right), \tag{1b}$$

Where $\langle D_\Gamma\rangle$ and $\langle \delta D_\Gamma(t)\delta D_\Gamma(0)\rangle$ denote, respectively, the mean and the time-correlation-function (TCF) of the effective diffusion coefficient fluctuation of the MPM. In eq 1, $\langle x'^2\rangle$ and $\alpha_2\left(x'\right)$ designate the variance and NGP of the stationary distribution of vesicle's relative position with respect to the MPM (see Material and Methods and Figure S5).

Quantitative Analyses of MSD and NGP time-profiles

The MSD time-profile of the VMPM in forskolin-treated cells is quantitatively explained by

eq 1a (see Figure 2a). From this analysis, we extracted the average value of the effective diffusion coefficient of the MPM motion along the microtubule as $\langle D_{\Gamma} \rangle \cong 1.77 \times 10^{-2}\,\mu\text{m}^2/\text{s}$ in forskolin-treated cells. This is about half the value observed in normal cells, where $\langle D_{\Gamma} \rangle \cong 3.44 \times 10^{-2}\,\mu\text{m}^2/\text{s}$. On the other hand, the variance in the vesicle's relative position with respect to the MPM is estimated to be $\langle x'^2 \rangle \cong 8.30 \times 10^{-3}\,\mu\text{m}^2$ in forskolin-treated cells, which is more than six times the variance in normal cells ($\langle x'^2 \rangle \cong 1.25 \times 10^{-3}\,\mu\text{m}^2$).

An accurate quantitative analysis of the NGP time-profile of VMPM motion is not an easy task. To analyze the NGP time-profile using eq 1b, we need a functional form of $\langle \delta D_{\Gamma}(t) \delta D_{\Gamma}(0) \rangle$, which depends on stochastic properties of the MPM motility fluctuation. It is often assumed that a TCF is a simple exponential function or a linear combination of a few exponential functions; however, this assumption is inconsistent with our experimental data, as discussed later. It is difficult to construct an accurate model at this stage due to the lack of information.

Instead of assuming a particular model of the MPM motility fluctuation from the beginning, we first extract the accurate time-profile of $\langle \delta D_{\Gamma}(t) \delta D_{\Gamma}(0) \rangle$ from our experimental data using

$$\left\langle \delta D(t) \delta D(0) \right\rangle = 8^{-1} \frac{d^2}{dt^2} \left[\left\langle d_x^2(t) \right\rangle^2 \alpha_{2,x}(t) \right], \qquad (2)$$

which can be easily obtained from eqs 1a and 1b. We emphasize that eq 2 enables us to extract the TCF of the MPM diffusion coefficient fluctuation directly from our experimental results for the MSD and NGP (see inset of Figure 2b), without assuming a specific model of the MPM motility fluctuation. As shown in the inset of Figure 2b, $\langle \delta D_{\Gamma}(t) \delta D_{\Gamma}(0) \rangle$ extracted from our experimental results using eq 2 has a non-monotonic time-dependence and a finite long-time saturation value.

Partially dynamic MPM motility fluctuation

The extracted time-profile of $\langle \delta D_{\Gamma}(t) \delta D_{\Gamma}(0) \rangle$ provides information useful for constructing a more explicit model of the MPM motility fluctuation. The long-time saturation of $\langle \delta D_{\Gamma}(t) \delta D_{\Gamma}(0) \rangle$ to a plateau value signifies that a group of MPMs has a static heterogeneity in the diffusion coefficient or dynamic heterogeneity whose relaxation occurs at times longer than our observation time.[65] The simple one-state model or the two-state dynamic model, $\Gamma_0 \rightleftarrows \Gamma_1$, of the MPM with a state-dependent motility cannot explain the long-time saturation of $\langle \delta D_{\Gamma}(t) \delta D_{\Gamma}(0) \rangle$ (Figure 3). In contrast, any model assuming an entirely static distribution of the MPM motility yields $\langle \delta D_{\Gamma}(t) \delta D_{\Gamma}(0) \rangle$ constant in time, which does not exhibit a time-dependent relaxation.

We could quantitatively explain the time-profile of $\langle \delta D_{\Gamma}(t) \delta D_{\Gamma}(0) \rangle$ using a model that accounts for both static heterogeneity and dynamic heterogeneity in the MPM motility. A minimalistic, quantitative model is as follows. The MPM-microtubule system comprises two different groups. In one group, MPMs have a dynamically fluctuating motility, whose value changes over time depending on the MPM-microtubule state. In the other group, MPMs have a motility with negligible temporal fluctuations. A schematic representation of this model is given by

$$\Gamma_0 \underset{\psi_1(t)}{\overset{\psi_0(t)}{\rightleftarrows}} \Gamma_1 \qquad \Gamma_2, \tag{3}$$

where Γ_0, Γ_1, and Γ_2 represent the MPM-microtubule states, which will be simply designated by the MPM states from now on. Throughout, D_j denotes the diffusion coefficient of the MPM at

state Γ_j. Reversible transitions occur between states Γ_0 and Γ_1, but there is no transition to or from state Γ_2, at least in our experimental time scale. $\psi_0(t)$ and $\psi_1(t)$ denote the lifetime distribution of state Γ_0 and state Γ_1, respectively.

For the model in eq 3, the analytic expression of $\langle \delta D_{\Gamma}(t)\delta D_{\Gamma}(0)\rangle$ is given by

$$\langle \delta D_{\Gamma}(t)\delta D_{\Gamma}(0)\rangle = \sum_{i=0}^{1}\sum_{j=0}^{1} D_i G(\Gamma_i, t\,|\,\Gamma_j) D_j p_j + D_2^2 p_2 - \langle D_{\Gamma}\rangle^2, \qquad (4)$$

where p_j denotes the equilibrium probability of state Γ_j, satisfying the normalization condition, $\sum_{j=0}^{2} p_j = 1$ (see Material and Methods). In eq 4, $G(\Gamma_i, t\,|\,\Gamma_j)$ denotes the probability that the MPM is at state Γ_i at time *t*, given that the MPM is initially at state Γ_j. An explicit analytic expression of $G(\Gamma_i, t\,|\,\Gamma_j)$ is available as a functional of $\psi_0(t)$ and $\psi_1(t)$ (see eq S3 in Supporting Information Section 2.1).[75] eq 1 with $\langle \delta D_{\Gamma}(t)\delta D_{\Gamma}(0)\rangle$ given by eq 4 provides a quantitative explanation of our experimental results for the time-profiles of the MSD and NGP of VMPM motion (Figures 2a and b). The optimized parameter values are given in Table 1 (see Material and Methods).

Prediction of the VMPM displacement distribution

Using our optimized model of VMPM motion in the hyperphosphorylated cells, we predicted the spatial profile of the VMPM displacement distribution (VDD) (see Material and Methods). The predictions of eqs 13, 14, and 16 in Material and Methods for our model are in quantitative agreement with the experimentally measured VDD at various times (Figure 2d). This remarkable agreement between theoretical prediction and experimental result for the VDD in our cell system show that our model, which accounts for both static and dynamic motility fluctuations

of the MPMs and the liberational motion of vesicle around the MPM, captures the essential features of the vesicle motion along the microtubule in hyperphosphorylated cells.

DISCUSSION

The hyperphosphorylation of tau suppresses the fast, long-distance vesicle transport of the motor proteins along the microtubule. This is because unidirectional motion of the MPM, which delivers vesicles faster over a long distance than bidirectional random motion, is negligible on the microtubule under tau-hyperphosphorylation. The suppression of unidirectional motion of the MPM is also manifested on vesicle trajectories in forskolin-treated cells (Figure S4) and the spatial profile of VDD in forskolin-treated cells. Because the unidirectional motion causes the VDD to deviate from Gaussian, the VDD in normal cells has a strongly non-Gaussian heavy tail, which is absent in the VDD in forskolin-treated cells (Figure S6).[17] Together, these results clearly shows that the fast, long-distance vesicle transport via unidirectional MPM motion is negligible in forskolin-treated cells.

A plausible mechanism of the hyperphosphorylation-induced change in MPM motion along the microtubule is a destabilization or structural change of the microtubule due to detachment of tau proteins from the microtubule upon hyperphosphorylation. Recent single molecule experiments clearly showed that tau proteins, which stabilize the helical structure of the microtubule, detach from the microtubule upon hyperphosphorylation,[76, 77] which is expected to deteriorate the structural stability of the microtubule. Other possible mechanisms of the change in the MPM motion include a structural change in the vesicle-MPM complex and a change in the dynamics of the ATP-hydrolysis catalyzed by the motor proteins. However, according to literature in this fields, the hyperphosphorylation induced destabilization of the microtubule seems the

primary cause of the loss of the change in the MPM motion on the microtubule upon hyperphosphorylation.

The loss of fast synaptic vesicle delivery by unidirectional MPM motion may be a mechanism of neurodegenerative disorders. The tau-hyperphosphorylation not only deteriorates the structural stability of neuronal cells,[76, 77] but also suppresses fast, long-distance delivery of synaptic vesicles by motor proteins along the microtubule, which would disrupt neuronal communications and brain functions. This may be a mechanism of neurodegenerative diseases associated with tau-hyperphosphorylation.[78]

In our forskolin-treated cells, the mean diffusion coefficient of MPMs moving along the microtubule is estimated to be $\langle D_{\Gamma} \rangle \cong 1.77 \times 10^{-2} \mu m^2/s$, far smaller than the diffusion coefficient value, $1.27 \times 10^{-1} \mu m^2/s$, of dilute vesicles in cytoplasm.[79] On the other hands, the standard deviation of vesicle's relative position with respect to the MPM is $\sqrt{\langle x'^2 \rangle} \cong 0.091$ μm in forskolin-treated cells, which is about three-times greater than that in normal cells (Figure S5). For this reason, VMPMs in forskolin-treated cells have greater MSD values at short times than VMPMs in normal cells (Figure 2a).

We emphasize that eq 2 is applicable to various probe-attached systems exhibiting non-Gaussian diffusion, which enables one to extract the TCF of the system's motility fluctuation from the MSD and NGP of probe particle, without any prior knowledge or assumptions. By using this method, we estimate the normalized standard deviation, $\sigma_D / \langle D_{\Gamma} \rangle$, of the MPM diffusion coefficient to be about 2.1 and extract the non-monotonic time profile of the TCF,

$\phi_D(t)\left[\equiv \langle \delta D_{\Gamma}(t)\delta D_{\Gamma}(0)\rangle / \sigma_D^2\right]$, of the diffusion coefficient fluctuation (inset of Figure 2b). The time-profile of $\phi_D(t)$, or the NGP time profile, carries a lot more information than the MSD time profile. As shown in Figure 3, the simple diffusion model of MPM motion, the dynamic two-state model, $\Gamma_0 \rightleftarrows \Gamma_1$, of the MPM with a state-dependent diffusion coefficient, and the static, three-state model of the MPM can all quantitatively explain the MSD time-profile of the VMPM, which obeys eq 1a. These models, however, cannot explain the time-profile of $\phi_D(t)$ or the NGP time-profile. In contrast, our MPM model with the partially dynamic MPM motility fluctuation, represented by eq 3, provides a simultaneous, quantitative explanation of the time profiles of $\phi_D(t)$, MSD, and NGP. According to our analysis, about 37% of MPMs exhibit temporal motility fluctuation while the remaining 63% of MPMs show negligible motility fluctuation (Table 1). We can think of more elaborated models of the MPM motion in hyperphosphorylated cells than ours. However, in this work, we choose arguably the simplest that quantitatively explains our experimental results. If we further simplify our model, we cannot explain the time-profiles of $\langle \delta D_{\Gamma}(t)\delta D_{\Gamma}(0)\rangle$ and the NGP (Figures 3 and S7).

Our model captures the essential features of the VMPM motion, but it should be improved to provide a more detailed explanation of our experimental results. Particularly, our model of the MPM motion cannot explain the emergence of the small second peak in the NGP time profile, which appears at about 10 seconds (Figure 2b). This indicates that the MPM motility fluctuation is far more complicated than assumed in our three-state model. We leave the improvement of our model for future research.

Finally, we discuss the effects of UCNPs on biological functions of cells according to an

anonymous reviewer's request. The size and surface coating of UCNPs can influence their cyto-toxicity.[80-82] The larger nanoparticles tend to induce greater cyto-toxicity.[83] It has been reported that polyacrylic acid (PAA)-coated UCNPs exhibit particularly lower cyto-toxicity towards various cell lines than bare UCNPs.[64] For this reason, we have employed the PAA-coated UCNP probe in this work. Although it was not observed in our cell system, endocytosed UCNPs can induce oxidative stress, inflammation and other immune responses including autophagy or apoptosis. Currently, these biological consequences of UCNPs are exploited for a variety of biomedical applications,[84] including the photodynamic therapy,[85-87] immunotherapy,[88] and noninvasive photochemical tissue bonding.[89]

This work demonstrates an effective approach to quantitative investigation into dynamics of complex systems. For a complex system, an experimental observable is often coupled with hidden dynamical variables about which we do not have much information. In this case, it is difficult to construct an explicit and accurate model from the beginning. However, if robust information about hidden variables coupled to our observable can be extracted by analyzing experimental data using a general theory, this information is useful for constructing a quantitative model of the complex system.[90]

CONCLUSIONS

We shed lights on how tau-hyperphosphorylation affects the vesicle-motor-protein-multiplex motion along the microtubule in living cells. Upon tau-hyperphosphorylation in neuronal cells, the fast, long-distance cargo delivery via unidirectional MPM motion is suppressed. In our experimental time scale, MPMs exhibit a non-Gaussian diffusion due to partially dynamic motility fluctuations; about 37% of MPMs exhibit dynamic motility

fluctuation and the remaining 63% static motility fluctuation in our experimental time window. The TCF of the diffusion coefficient fluctuation can be extracted from the MSD and NGP time profiles using eq 2; the TCF of the MPM diffusion coefficient fluctuation exhibits a unique, non-monotonic time-dependence. Using this information, we construct a minimalistic model that provides a simultaneous, quantitative explanation of the TCF of the MPM diffusion coefficient fluctuation, the MSD and NGP time-profiles of VMPM and even accurate predictions for the VMPM displacement distribution at various times for the VMPM moving along the microtubule in living cells under hyperphosphorylation conditions. The mean diffusion coefficient of the vesicle carried by MPMs on unstable microtubules is estimated to be $\langle D_{\Gamma} \rangle \cong 1.77 \times 10^{-2}\,\mu m^2/s$, only 14% of the diffusion coefficient of dilute vesicles undergoing thermal motion in cytoplasm. The normalized standard deviation, $\sigma_D / \langle D_{\Gamma} \rangle$, of the MPM diffusion coefficient is about 2.1. The standard deviation of the vesicle position with respect to the MPM is approximately 0.091 μm in forskolin-treated cells, about three-times greater than that in normal cells. The loss of fast cargo delivery dynamics may be a functional mechanism of various neurodegenerative diseases associated with tau-hyperphosphorylation.

Supporting Information

The Supporting Information is available free of charge at https://pubs.acs.org/doi/

- Supplementary Materials and Methods, Theory and quantitative analysis of experimental data, and Supplementary Figures (PDF)
- Supplementary video: vesicle motion in hyperphosphorylated neuronal cells

MATERIAL AND METHODS

Cell system and imaging probe

SH-SY5Y cells were differentiated to neuronal phenotype by retinoic acid treatment (see Supporting Information Section 1). Then, the differentiated cells were treated by Forskolin to induce hyperphosphorylation of Tau. We confirm hyperphosphorylation of tau protein in our cells by Western blotting to estimate pTau-S214 and pTau-T231 levels (see Supporting Information Section 1.2). As the imaging probe, we adopted Yb^{3+}, Er^{3+} doped core/shell UCNPs ($NaY_{0.78}F_4:Yb^{3+}_{0.2}$, $\underline{Er^{3+}_{0.02}@NaYF_4@PAA}$). These probes have hexagonal structure and a 24.5 (±1.0) nm size (Figure S1) and have green (530 nm and 550 nm) and red emissions (650 nm) under 980 nm excitation (Figure S3a). For simultaneous, real-time tracking of multiple UCNP probes, we use the wide-field based epi-fluorescence microscope developed in our previous work[17] (Figure S3b).

MSD and NGP of the VMPM

The displacement of the MPM and the change in the relative motion of the vesicle with respect to the MPM are not strongly correlated. Therefore, the second and fourth moments of vesicle displacement are given by

$$\langle d_x^2(t)\rangle = \langle R_x^2(t)\rangle + \langle x'^2\rangle, \tag{5a}$$

$$\langle d_x^4(t)\rangle = \langle R_x^4(t)\rangle + \langle x'^4\rangle + 6\langle R_x^2(t)\rangle\langle x'^2\rangle, \tag{5b}$$

where $\langle R_x^n(t)\rangle$ and $\langle x'^n\rangle$ denote, respectively, the *n*th moment of the MPM displacement distribution and the *n*th moment of the distribution of vesicle's relative displacement with respect

to the MPM. The MSD of the VMPM designates $\langle d_x^2(t)\rangle$ given in eq 5a.

Substituting eqs 1a and 1b into the definition of the non-Gaussian parameter (NGP), $[\langle d_x^4(t)\rangle / 3\langle d_x^2(t)\rangle^2] - 1$, we obtain a general expression of the NGP of the VMPM displacement,

$$\alpha_{2,x}(t) = \frac{\langle R_x^2(t)\rangle^2}{\langle d_x^2(t)\rangle^2}\alpha_2\left(R_x, t\right) + \frac{\langle x'^2\rangle^2}{\langle d_x^2(t)\rangle^2}\alpha_2\left(x'\right), \tag{6}$$

where $\alpha_2(R_x, t)$ and $\alpha_2(x')$ represent, respectively, the NGP of the R_x distribution and the NGP of the x' distribution. In eqs 5 and 6, because x' assumes a stationary distribution in our experimental time resolution, $\langle x'^2\rangle$ and $\alpha_2(x')$ are set to be constant in time. On the other hand, the displacement of the MPM motion along the microtubule has a non-stationary distribution, so that the values of $\langle R_x^2(t)\rangle$ and $\alpha_2(R_x, t)$ change over time. We emphasize that eqs 5 and 6 are applicable not only to our VMPM system but also to any probe-attached system regardless of the system's transport dynamics. However, to analyze the NGP time profile using eq 6, we need an explicit functional form of $\langle R_x^2(t)\rangle$, which is dependent on a model of MPM motion along the microtubule.

Transport equation describing MPM motion along the microtubule in hyperphosphorylated cells

In our model, the MPM alternatingly undergoes unidirectional active motion and a random change in the direction of the active motion where the speed of the unidirectional MPM motion is dependent on the MPM state, Γ, which include the microtubule state. At time scales far longer than the time scale of the random change in the direction of the MPM motion, the probability distribution of the position and state of MPMs can be described by

$$\hat{\hat{p}}(x,\mathbf{\Gamma},s) = D_{\mathbf{\Gamma}} \frac{\partial^2}{\partial x^2} \hat{p}(x,\mathbf{\Gamma},s) + L(\mathbf{\Gamma})\hat{p}(x,\mathbf{\Gamma},s), \quad (7)$$

where $p(x,\mathbf{\Gamma},t)$ designates the joint probability density that an MPM is located at position x and the MPM is at state $\mathbf{\Gamma}$ at time t, satisfying the normalization condition: $\int_{-\infty}^{\infty} dx \int d\mathbf{\Gamma} p(x,\mathbf{\Gamma},t) = 1$. In eq 7, $\hat{p}(x,\mathbf{\Gamma},s)$ and $\hat{\hat{p}}(x,\mathbf{\Gamma},s)$ denote the Laplace transforms of $p(x,\mathbf{\Gamma},t)$ and $\partial_t p(x,\mathbf{\Gamma},t)$ with s being the Laplace variable. $D_{\mathbf{\Gamma}}$ and $L(\mathbf{\Gamma})$ in eq 7 denote, respectively, the effective diffusion coefficient of the MPM at state $\mathbf{\Gamma}$ and a mathematical operator describing dynamics of MPM state $\mathbf{\Gamma}$. At this stage, we do not have information about the MPM-state dynamics required to construct an explicit mathematical form of operator $L(\mathbf{\Gamma})$. However, by analyzing our experimental results using a general solution of eq 7, we obtain the analytic expressions for the MSD and NGP of the VMPM and extract information about the MPM state dynamics and the mathematical form of $L(\mathbf{\Gamma})$, as demonstrated in the main text. Equation 7 can also be derived by considering the continuum limit of an unbiased random walk of the MPM, in which the speed of the unidirectional motion of the MPM to the nearest neighbor site on the microtubule is not a constant but a function of MPM state $\mathbf{\Gamma}$ (see Supporting Information Section 2.5). We also note there that eq 7 is a limiting form of the general transport equation describing non-Fickian and non-Gaussian motion in complex systems,[65, 91] which can be derived either by considering the environmental state dependent continuous time random walk model or by applying the projection operator technique to a general many-particle system that obeys Newton's classical dynamics.[92, 93]

Mean square displacement and the non-Gaussian parameter of MPM motion

From eq 7, we obtain the general analytic expression for the second and fourth moments,

$\langle R_x^2(t)\rangle (\equiv \langle [R_x(t)-R_x(0)]^2\rangle)$ and $\langle R_x^4(t)\rangle (\equiv \langle [R_x(t)-R_x(0)]^4\rangle)$, of the MPM displacement using the similar mathematical method as ref.[65]. The analytic results are given by

$$\langle R_x^2(t)\rangle = 2\langle D_\Gamma\rangle t, \tag{8a}$$

$$\langle R_x^4(t)\rangle = 3\langle R_x^2(t)\rangle^2 + 24\int_0^t d\tau (t-\tau)\langle \delta D_\Gamma(\tau)\delta D_\Gamma(0)\rangle, \tag{8b}$$

where $\langle D_\Gamma\rangle$ and $\langle \delta D_\Gamma(\tau)\delta D_\Gamma(0)\rangle$ denotes, respectively, the mean and the time correlation function (TCF) of the diffusion coefficient fluctuation of the MPM moving along the microtubule in hyperphosphorylated cells.

Substituting eqs 8a and 8b into the definition of the NGP, $\alpha_2(R_x,t)[\equiv \langle R_x^4\rangle / (3\langle R_x^2(t)\rangle^2) - 1]$, of the MPM displacement, we obtain

$$\alpha_2(R_x,t) = 2\eta_D^2 t^{-2}\int_0^t d\tau (t-\tau)\phi_D(\tau), \tag{9a}$$

where η_D^2 and $\phi_D(\tau)$ denotes the relative variance and the normalized TCF of the diffusion coefficient fluctuation, defined by $\eta_D^2 \equiv \langle \delta D_\Gamma^2\rangle / \langle D_\Gamma\rangle^2$ and $\phi_D(\tau) = \langle \delta D_\Gamma(\tau)\delta D_\Gamma(0)\rangle / \langle \delta D_\Gamma^2\rangle$. Substituting eqs 8a and 9a into the eqs 5 and 6, we obtain eq 1 in the main text. At short times where $\phi_D(\tau) \cong 1$, the NGP given in eq 9a becomes approximately the same as η_D^2, i.e., $\alpha_2(R_x,t) \cong \eta_D^2$. In contrast, at long times, the NGP has the following asymptotic behavior:

$$\alpha_2(R_x,t) \cong \eta_D^2\phi_D(\infty) + 2\eta_D^2 t_D/t, \tag{9b}$$

where t_D is the relaxation time of the diffusion coefficient fluctuation, defined by $t_D \equiv \int_0^\infty d\tau [\phi_D(\tau) - \phi_D(\infty)]$.

The long-time limit value of $\alpha_2(R_x,t)$ is finite only when $\phi_D(t)$ does not vanish at long times. From eq 9b, one can see that $\lim_{t\to\infty}\alpha_2(R_x,t)=\phi_D(\infty)\eta_D^2$, likewise one can obtain asymptotic behavior of the non-Gaussian parameter of the vesicle-motor protein multiplex (see Supporting Information Section 2.2). $\phi_D(\infty)$ has a finite value only when the MPM motility depends on the MPM state and there exists an MPM state or a group of MPM states from or to which no transition occurs.

Analytic expression for the TCF of the diffusion coefficient fluctuation

The time-correlation function of the diffusion coefficient is defined by

$$\langle D_{\mathbf{\Gamma}}(t)D_{\mathbf{\Gamma}}(0)\rangle=\int d\Gamma\int d\Gamma_0 D_{\Gamma}G(\Gamma,t\,|\,\Gamma_0)D_{\Gamma_0}p_I(\Gamma_0), \tag{10}$$

where $G(\Gamma,t\,|\,\Gamma_0)$ denotes the probability that the MPM state is found at Γ at time *t*, given that the MPM is initially at state Γ_0. $p_I(\Gamma_0)$ denotes the probability that the MPM is initially at state Γ_0. The TCF of the diffusion coefficient fluctuation, $\delta D_{\mathbf{\Gamma}}(t)=D_{\mathbf{\Gamma}}(t)-\langle D_{\mathbf{\Gamma}}\rangle$, is given by

$$\langle \delta D_{\mathbf{\Gamma}}(t)\delta D_{\mathbf{\Gamma}}(0)\rangle=\langle D_{\mathbf{\Gamma}}(t)D_{\mathbf{\Gamma}}(0)\rangle-\langle D_{\mathbf{\Gamma}}\rangle^2. \tag{11}$$

For our discrete MPM state model given in eq 3, eqs 10 and 11 yield eq 4 in the main text, and the analytic expression of $G(\Gamma_i,t\,|\,\Gamma_j)$ in the Laplace domain is given in Supporting Information Section 2.1, eq S3

Quantitative model of MPM motion in hyperphosphorylated cells.

The time-profile of $\langle \delta D_{\mathbf{\Gamma}}(t)\delta D_{\mathbf{\Gamma}}(0)\rangle$ extracted from our analysis of experimental data is quantitatively explained by eq 4, obtained for the model of MPM motion in eq 3, if the MPM state

lifetime distributions, $\psi_0(t)$ and $\psi_1(t)$, are assumed to be gamma distributions (Figure S8). The mean and relative variance of the MPM state lifetimes are extracted as $\langle t_0 \rangle \cong 2.85$s and $\langle \delta t_0^2 \rangle / \langle t_0 \rangle^2 \cong 0.14$ for state Γ_0 and $\langle t_1 \rangle \cong 1.34$s and $\langle \delta t_1^2 \rangle / \langle t_1 \rangle^2 \cong 0.74$ for state Γ_1. According to these results, the transitions between the MPM states are sub-Poisson processes for which the relative variance of the MPM state lifetime is less than unity. The sub-Poisson state transition dynamics emerges when the state transition is a multi-step process.[94] The non-monotonic time dependence of the normalized TCF of the diffusion coefficient fluctuation, $\phi_D(t)\left[\equiv \langle \delta D_\Gamma(t) \delta D_\Gamma(0) \rangle / \langle \delta D_\Gamma^2 \rangle\right]$, shown in inset of Figure 2b, results from the sub-Poisson MPM state transition processes. $\langle \delta D_\Gamma(t) \delta D_\Gamma(0) \rangle$ would have monotonically decreased with time if the transitions between the MPM states were Poisson processes or first-order kinetic processes with constant rate coefficients (Figure S7) or if they were super-Poisson processes or multi-channel processes.

Distribution of a vesicle's position relative to the MPM carrying the vesicle

The relative position of a vesicle with respect to the MPM assumes a stationary distribution in our experimental time resolution, 0.1 seconds. We obtain the stationary distribution of vesicle position with respect to the MPM from the VDD at short times at which MPM motion is negligible (Figure S5). The experimentally observed stationary distribution of vesicle around the MPM can be explained by the following superposition of Gaussians with heterogeneous variance[17]:

$$f(x') = \int_{-\infty}^{\infty} dq \sqrt{\frac{\kappa_0}{2\pi(1+q^2)}} \exp\left(-\frac{\kappa_0 x'^2}{2(1+q^2)} \right) N(q \mid \sigma_q^2), \qquad (12)$$

where κ_0 and σ_q^2 are constant (Figure S5). In eq 12, $N(q \mid \sigma_q^2)$ denotes the normal distribution of

q with zero mean and variance σ_q^2 . The optimized parameter values are given by $\kappa_0^{-1} = 2.4\times10^{-3}\mu\text{m}^2$ and $\sigma_q^2 = 2.46$. The variance, $\langle x'^2\rangle$, and NGP, $\alpha_2(x')$, are given by $\kappa_0^{-1}(1+\sigma_q^2)\left(\cong 0.0083\mu\text{m}^2\right)$ and $2\sigma_q^4/\left(1+\sigma_q^2\right)^2\left(\cong 1.0096\right)$ respectively. The Fourier transform of eq 12 is given by

$$\tilde{f}(k) = \exp\left(-k^2/2\kappa_0\right)\Big/\sqrt{\sigma_q^2\left(k^2/\kappa_0\right)+1}\,. \tag{13}$$

with k denoting the Fourier variable, i.e., $\tilde{f}(k) = \int_{-\infty}^{\infty} dx' e^{-ikx'} f(x')$.

Distribution of the MPM displacement

For our MPM model given in eq 3, we obtain the analytic expression for the MPM displace distribution (see Supporting Information Section 2.3) in the Fourier-Laplace transform domain, which read as

$$\hat{\tilde{P}}(k,s) = -\left(1-p_2\right)\frac{\left[1-\hat{\psi}_0(s_0)\right]\left[1-\hat{\psi}_1(s_1)\right]}{\left(\langle t_0\rangle+\langle t_1\rangle\right)\left[1-\hat{\psi}_0(s_0)\hat{\psi}_1(s_1)\right]}\left(\frac{1}{s_0}-\frac{1}{s_1}\right)^2+\frac{p_0}{s_0}+\frac{p_1}{s_1}+\frac{p_2}{s_2}\,, \tag{14}$$

where $\hat{\tilde{P}}(k,s)$ designates the Fourier-Laplace transform of the MPM displacement distribution, $P(R_x,t)$, i.e., $\hat{\tilde{P}}(k,s) = \int_{-\infty}^{\infty} dR_x \exp(ikR_x)\int_0^{\infty} ds \exp(-st)P(R_x,t)$ and s_i denotes $s+D_i k^2$ with s and k denoting the Laplace variable and the Fourier variable, respectively In eq 14, p_i denotes the equilibrium probability of MPM state Γ_i, which satisfies $\sum_{i=0}^{2} p_i = 1$, and p_0 and p_1 are dependent on the mean lifetimes of Γ_0 and Γ_1 and p_2 , i.e., $p_0 = (1-p_2)\langle t_0\rangle/\left(\langle t_0\rangle+\langle t_1\rangle\right)$ and $p_1 = (1-p_2)\langle t_1\rangle/\left(\langle t_0\rangle+\langle t_1\rangle\right)$ with $\langle t_0\rangle$ and $\langle t_1\rangle$ being the mean lifetime of MPM state 0 and 1,

that is, $\langle t_i \rangle = \int_0^\infty dt\ t\psi_i(t)$.

Analytic expression of the vesicle displacement distribution in hyperphosphorylated cells

Given that the position of a vesicle can be represented by $d_x = R_x + x'$ where R_x and x' denote, respectively, the position of the MPM and the relative position of the vesicle with respect to the MPM, the displacement distribution $g(d_x, t)$ of the vesicle-MPM along the microtubule can be written

$$\begin{aligned} g(d_x,t) &= \int_{-\infty}^{\infty} dR_x \int_{-\infty}^{\infty} dx' \delta(d_x - R_x - x') P(R_x,t) f(x') \\ &= \int_{-\infty}^{\infty} dx' P(d_x - x', t) f(x') \end{aligned}, \qquad (15)$$

where $\delta(x)$, $P(R_x, t)$ and $f(x')$ denote, respectively, Dirac's delta function, the distribution of the MPM displacement, and the distribution of the relative position x', of the vesicle with respect to the MPM. Taking the Fourier-Laplace transform of eq 15, we obtain

$$\hat{\tilde{g}}(k,s) = \hat{\tilde{P}}(k,s)\tilde{f}(k), \qquad (16)$$

This equation with eqs 13 and 14 provides the analytic expression of the displacement distribution of the vesicle transported by MPM in the Fourier-Laplace domain.

We confirm the correctness of eq 16 against an accurate stochastic simulation result for our model (Figure S9). Numerical inversion[95] of eq 16 using the optimized parameter values in Table 1 allows us to predict the spatial profile of the vesicle displacement distribution. As shown in Figure 2d, our theoretical prediction is in excellent agreement with the experimental results for the vesicle displacement distribution.

Acknowledgments

K.T.L. was supported by the grant awarded from GIST in 2020 through the Research Institute (GRI) program and by the National Research Foundation (NRF) of S. Korea (Grant no. 2020R1F1A1073442, 2021R1A2C2010557). J.S. was supported by the Creative Research Initiative Project Program (NRF-2015R1A3A2066497) and the Engineering Research Center Program funded by the Korea government (MSIT) (NRF-2020R1A5A1018052). Y.H.S., J.-H.K., and M.H.L. were supported by the NRF [NRF-2019R1I1A1A01056975 (Y.H.S.); NRF-2020R1A2C1102788 (J.-H.K.); NRF-2022R1A3B1077319 (M.H.L.)].

References

(1) Hirokawa, N.; Noda, Y.; Tanaka, Y.; Niwa, S. Kinesin superfamily motor proteins and intracellular transport. *Nat. Rev. Mol. Cell Biol.* **2009**, *10* (10), 682-696.
(2) Asbury, C. L.; Fehr, A. N.; Block, S. M. Kinesin moves by an asymmetric hand-over-hand mechanism. *Science* **2003**, *302* (5653), 2130-2134.
(3) Vershinin, M.; Carter, B. C.; Razafsky, D. S.; King, S. J.; Gross, S. P. Multiple-motor based transport and its regulation by Tau. *Proc. Natl. Acad. Sci. U.S.A.* **2007**, *104* (1), 87-92.
(4) Kaplan, L.; Ierokomos, A.; Chowdary, P.; Bryant, Z.; Cui, B. Rotation of endosomes demonstrates coordination of molecular motors during axonal transport. *Sci. Adv.* **2018**, *4* (3), e1602170.
(5) Blehm, B. H.; Selvin, P. R. Single-molecule fluorescence and in vivo optical traps: how multiple dyneins and kinesins interact. *Chem. Rev.* **2014**, *114* (6), 3335-3352.
(6) Schimert, K. I.; Budaitis, B. G.; Reinemann, D. N.; Lang, M. J.; Verhey, K. J. Intracellular cargo transport by single-headed kinesin motors. *Proc. Natl. Acad. Sci. U.S.A.* **2019**, *116* (13), 6152-6161.
(7) Vale, R. D. The molecular motor toolbox for intracellular transport. *Cell* **2003**, *112* (4), 467-480.
(8) Baas, P. W.; Lin, S. Hooks and comets: The story of microtubule polarity orientation in the neuron. *Dev Neurobiol* **2011**, *71* (6), 403-418. DOI: 10.1002/dneu.20818.
(9) Baas, P. W.; Deitch, J. S.; Black, M. M.; Banker, G. A. Polarity orientation of microtubules in hippocampal neurons: uniformity in the axon and nonuniformity in the dendrite. *Proc. Natl. Acad. Sci. U.S.A.* **1988**, *85* (21), 8335-8339.
(10) Chrétien, D.; Kenney, J. M.; Fuller, S. D.; Wade, R. H. Determination of microtubule polarity by cryo-electron microscopy. *Structure* **1996**, *4* (9), 1031-1040.
(11) Shelley, M. J. The Dynamics of Microtubule/Motor-Protein Assemblies in Biology and Physics. *Annu. Rev. Fluid Mech.* **2016**, *48* (1), 487-506. DOI: 10.1146/annurev-fluid-010814-013639.
(12) Fürthauer, S.; Lemma, B.; Foster, P. J.; Ems-McClung, S. C.; Yu, C.-H.; Walczak, C. E.; Dogic, Z.; Needleman, D. J.; Shelley, M. J. Self-straining of actively crosslinked microtubule networks. *Nat. Phys.* **2019**, *15* (12), 1295-1300.
(13) Nan, X.; Sims, P. A.; Xie, X. S. Organelle tracking in a living cell with microsecond time resolution and nanometer spatial precision. *ChemPhysChem* **2008**, *9* (5), 707-712.
(14) Sims, P. A.; Xie, X. S. Probing dynein and kinesin stepping with mechanical manipulation in a living cell. *ChemPhysChem* **2009**, *10* (9-10), 1511-1516.
(15) Klumpp, S.; Lipowsky, R. Cooperative cargo transport by several molecular motors. *Proc. Natl. Acad. Sci. U.S.A.* **2005**, *102* (48), 17284-17289.
(16) Müller, M. J.; Klumpp, S.; Lipowsky, R. Tug-of-war as a cooperative mechanism for bidirectional cargo transport by molecular motors. *Proc. Natl. Acad. Sci. U.S.A.* **2008**, *105* (12), 4609-4614.
(17) Shin, K.; Song, S.; Song, Y. H.; Hahn, S.; Kim, J.-H.; Lee, G.; Jeong, I.-C.; Sung, J.; Lee, K. T. Anomalous dynamics of in vivo cargo delivery by motor protein multiplexes. *J. Phys. Chem, Lett.* **2019**, *10* (11), 3071-3079.

(18) Hirokawa, N. Kinesin and dynein superfamily proteins and the mechanism of organelle transport. *Science* **1998**, *279* (5350), 519-526.
(19) Kural, C.; Kim, H.; Syed, S.; Goshima, G.; Gelfand, V. I.; Selvin, P. R. Kinesin and dynein move a peroxisome in vivo: a tug-of-war or coordinated movement? *Science* **2005**, *308* (5727), 1469-1472.
(20) Hancock, W. O. Bidirectional cargo transport: moving beyond tug of war. *Nat. Rev. Mol. Cell Biol.* **2014**, *15* (9), 615-628.
(21) Chen, K.; Wang, B.; Granick, S. Memoryless self-reinforcing directionality in endosomal active transport within living cells. *Nat. Mater.* **2015**, *14* (6), 589-593.
(22) Nan, X.; Sims, P. A.; Chen, P.; Xie, X. S. Observation of individual microtubule motor steps in living cells with endocytosed quantum dots. *J. Phys. Chem. B* **2005**, *109* (51), 24220-24224.
(23) Cui, B.; Wu, C.; Chen, L.; Ramirez, A.; Bearer, E. L.; Li, W.-P.; Mobley, W. C.; Chu, S. One at a time, live tracking of NGF axonal transport using quantum dots. *Proc. Natl. Acad. Sci. U.S.A.* **2007**, *104* (34), 13666-13671.
(24) Chowdary, P. D.; Che, D. L.; Kaplan, L.; Chen, O.; Pu, K.; Bawendi, M.; Cui, B. Nanoparticle-assisted optical tethering of endosomes reveals the cooperative function of dyneins in retrograde axonal transport. *Sci. Rep.* **2015**, *5* (1), 1-11.
(25) Song, M. S.; Moon, H. C.; Jeon, J.-H.; Park, H. Y. Neuronal messenger ribonucleoprotein transport follows an aging Lévy walk. *Nat. Commun.* **2018**, *9* (1), 1-8.
(26) Park, S. J.; Song, S.; Jeong, I.-C.; Koh, H. R.; Kim, J.-H.; Sung, J. Nonclassical kinetics of clonal yet heterogeneous enzymes. *J. Phys. Chem, Lett.* **2017**, *8* (13), 3152-3158.
(27) Avila, J.; Lucas, J. J.; Perez, M.; Hernandez, F. Role of tau protein in both physiological and pathological conditions. *Physiol. Rev.* **2004**.
(28) Khatoon, S.; Grundke-Iqbal, I.; Iqbal, K. Brain levels of microtubule-associated protein τ are elevated in Alzheimer's disease: A radioimmuno-slot-blot assay for nanograms of the protein. *J. Neurochem.* **1992**, *59* (2), 750-753.
(29) Khatoon, S.; Grundke-Iqbal, I.; Iqbal, K. Levels of normal and abnormally phosphorylated tau in different cellular and regional compartments of Alzheimer disease and control brains. *FEBS Lett.* **1994**, *351* (1), 80-84.
(30) Arendt, T.; Stieler, J. T.; Holzer, M. Tau and tauopathies. *Brain Res. Bull.* **2016**, *126*, 238-292.
(31) Goedert, M.; Spillantini, M. G.; Jakes, R.; Rutherford, D.; Crowther, R. Multiple isoforms of human microtubule-associated protein tau: sequences and localization in neurofibrillary tangles of Alzheimer's disease. *Neuron* **1989**, *3* (4), 519-526.
(32) Alonso, A. d. C.; Zaidi, T.; Novak, M.; Grundke-Iqbal, I.; Iqbal, K. Hyperphosphorylation induces self-assembly of τ into tangles of paired helical filaments/straight filaments. *Proc. Natl. Acad. Sci. U.S.A.* **2001**, *98* (12), 6923-6928.
(33) Braak, H.; Alafuzoff, I.; Arzberger, T.; Kretzschmar, H.; Del Tredici, K. Staging of Alzheimer disease-associated neurofibrillary pathology using paraffin sections and immunocytochemistry. *Acta Neuropathol.* **2006**, *112* (4), 389-404.
(34) De Calignon, A.; Polydoro, M.; Suárez-Calvet, M.; William, C.; Adamowicz, D. H.; Kopeikina, K. J.; Pitstick, R.; Sahara, N.; Ashe, K. H.; Carlson, G. A. Propagation of tau pathology in a model of early Alzheimer's disease. *Neuron* **2012**, *73* (4), 685-697.

(35) Wang, Y.; Mandelkow, E. Tau in physiology and pathology. *Nat. Rev. Neurosci.* **2016**, *17* (1), 22-35.
(36) Lesné, S.; Koh, M. T.; Kotilinek, L.; Kayed, R.; Glabe, C. G.; Yang, A.; Gallagher, M.; Ashe, K. H. A specific amyloid-β protein assembly in the brain impairs memory. *Nature* **2006**, *440* (7082), 352-357.
(37) Piller, C. Blots on a field? *Science (New York, NY)* **2022**, *377* (6604), 358-363.
(38) Wang, J.-z.; Wu, Q.; Smith, A.; Grundke-Iqbal, I.; Iqbal, K. τ is phosphorylated by GSK-3 at several sites found in Alzheimer disease and its biological activity markedly inhibited only after it is prephosphorylated by A-kinase. *FEBS Lett.* **1998**, *436* (1), 28-34.
(39) Falcon, B.; Cavallini, A.; Angers, R.; Glover, S.; Murray, T. K.; Barnham, L.; Jackson, S.; O'Neill, M. J.; Isaacs, A. M.; Hutton, M. L. Conformation determines the seeding potencies of native and recombinant Tau aggregates. *J. Biol. Chem.* **2015**, *290* (2), 1049-1065.
(40) Gendron, T. F.; Petrucelli, L. The role of tau in neurodegeneration. *Mol. Neurodegener.* **2009**, *4*, 1-19.
(41) Houck, A. L.; Hernández, F.; Ávila, J. A simple model to study tau pathology. *J. Exp. Neurosci.* **2016**, *10*, JEN. S25100.
(42) Min, S.-W.; Chen, X.; Tracy, T. E.; Li, Y.; Zhou, Y.; Wang, C.; Shirakawa, K.; Minami, S. S.; Defensor, E.; Mok, S. A. Critical role of acetylation in tau-mediated neurodegeneration and cognitive deficits. *Nat. Med.* **2015**, *21* (10), 1154-1162.
(43) Irwin, D. J. Tauopathies as clinicopathological entities. *Parkinsonism Relat. Disord.* **2016**, *22*, S29-S33.
(44) Binder, L. I.; Guillozet-Bongaarts, A. L.; Garcia-Sierra, F.; Berry, R. W. Tau, tangles, and Alzheimer's disease. *Biochim. Biophys. Acta Mol. Basis Dis.* **2005**, *1739* (2-3), 216-223.
(45) De Vos, K. J.; Grierson, A. J.; Ackerley, S.; Miller, C. C. Role of axonal transport in neurodegenerative diseases. *Annu. Rev. Neurosci.* **2008**, *31*, 151-173.
(46) Maday, S.; Twelvetrees, A. E.; Moughamian, A. J.; Holzbaur, E. L. Axonal transport: cargo-specific mechanisms of motility and regulation. *Neuron* **2014**, *84* (2), 292-309.
(47) Ebneth, A.; Godemann, R.; Stamer, K.; Illenberger, S.; Trinczek, B.; Mandelkow, E.-M.; Mandelkow, E. Overexpression of tau protein inhibits kinesin-dependent trafficking of vesicles, mitochondria, and endoplasmic reticulum: implications for Alzheimer's disease. *J. Cell Biol.* **1998**, *143* (3), 777-794.
(48) Vershinin, M.; Xu, J.; Razafsky, D. S.; King, S. J.; Gross, S. P. Tuning microtubule-based transport through filamentous MAPs: the problem of dynein. *Traffic* **2008**, *9* (6), 882-892.
(49) Chaudhary, A. R.; Berger, F.; Berger, C. L.; Hendricks, A. G. Tau directs intracellular trafficking by regulating the forces exerted by kinesin and dynein teams. *Traffic* **2018**, *19* (2), 111-121.
(50) Dixit, R.; Ross, J. L.; Goldman, Y. E.; Holzbaur, E. L. Differential regulation of dynein and kinesin motor proteins by tau. *Science* **2008**, *319* (5866), 1086-1089.
(51) Ahn, S.; Suh, J.-S.; Jang, Y.-K.; Kim, H.; Han, K.; Lee, Y.; Choi, G.; Kim, T.-J. TAUCON and TAUCOM: A novel biosensor based on fluorescence resonance energy transfer for detecting tau hyperphosphorylation-associated cellular pathologies. *Biosens. Bioelectron.* **2023**, *237*, 115533.
(52) Barkai, E.; Garini, Y.; Metzler, R. Strange kinetics of single molecules in living cells. *Phys. Today* **2012**, *65* (8), 29-35.

(53) Goychuk, I.; Kharchenko, V. O.; Metzler, R. Molecular motors pulling cargos in the viscoelastic cytosol: how power strokes beat subdiffusion. *Phys. Chem. Chem. Phys.* **2014**, *16* (31), 16524-16535.
(54) Park, H.; Toprak, E.; Selvin, P. R. Single-molecule fluorescence to study molecular motors. *Quarterly reviews of biophysics* **2007**, *40* (1), 87-111.
(55) Lim, S.; Haque, M. M.; Nam, G.; Ryoo, N.; Rhim, H.; Kim, Y. K. Monitoring of intracellular tau aggregation regulated by OGA/OGT inhibitors. *Int. J. Mol. Sci.* **2015**, *16* (9), 20212-20224.
(56) Liu, J.; Chesnokova, O.; Oleinikov, I.; Qiang, Y.; Oleinikov, A. V.; Du, E. Optimization of in vitro trophoblast assay for real-time impedimetric sensing of trophoblast-erythrocyte interactions in Plasmodium falciparum malaria. *Anal. Bioanal. Chem.* **2020**, *412*, 3915-3923.
(57) Hell, S. W.; Wichmann, J. Breaking the diffraction resolution limit by stimulated emission: stimulated-emission-depletion fluorescence microscopy. *Opt. Lett.* **1994**, *19* (11), 780-782.
(58) Betzig, E.; Chichester, R. J. Single molecules observed by near-field scanning optical microscopy. *Science* **1993**, *262* (5138), 1422-1425.
(59) Rust, M. J.; Bates, M.; Zhuang, X. Sub-diffraction-limit imaging by stochastic optical reconstruction microscopy (STORM). *Nat. Methods* **2006**, *3* (10), 793-796.
(60) Yildiz, A.; Forkey, J. N.; McKinney, S. A.; Ha, T.; Goldman, Y. E.; Selvin, P. R. Myosin V walks hand-over-hand: single fluorophore imaging with 1.5-nm localization. *science* **2003**, *300* (5628), 2061-2065.
(61) Gordon, M. P.; Ha, T.; Selvin, P. R. Single-molecule high-resolution imaging with photobleaching. *Proc. Natl. Acad. Sci. U.S.A.* **2004**, *101* (17), 6462-6465.
(62) English, B. P.; Min, W.; Van Oijen, A. M.; Lee, K. T.; Luo, G.; Sun, H.; Cherayil, B. J.; Kou, S.; Xie, X. S. Ever-fluctuating single enzyme molecules: Michaelis-Menten equation revisited. *Nat. Chem. Biol* **2006**, *2* (2), 87-94.
(63) Mao, X.; Liu, C.; Hesari, M.; Zou, N.; Chen, P. Super-resolution imaging of non-fluorescent reactions via competition. *Nat. Chem.* **2019**, *11* (8), 687-694.
(64) Rafique, R.; Baek, S. H.; Park, C. Y.; Chang, S.-J.; Gul, A. R.; Ha, S.; Nguyen, T. P.; Oh, H.; Ham, S.; Arshad, M. Morphological evolution of upconversion nanoparticles and their biomedical signal generation. *Sci. Rep.* **2018**, *8* (1), 17101.
(65) Song, S.; Park, S. J.; Kim, M.; Kim, J. S.; Sung, B. J.; Lee, S.; Kim, J.-H.; Sung, J. Transport dynamics of complex fluids. *Proc. Natl. Acad. Sci. U.S.A.* **2019**, *116* (26), 12733-12742. DOI: 10.1073/pnas.1900239116.
(66) Wang, B.; Anthony, S. M.; Bae, S. C.; Granick, S. Anomalous yet Brownian. *Proc. Natl. Acad. Sci. U.S.A.* **2009**, *106* (36), 15160. DOI: 10.1073/pnas.0903554106.
(67) Guan, J.; Wang, B.; Granick, S. Even hard-sphere colloidal suspensions display Fickian yet non-Gaussian diffusion. *ACS nano* **2014**, *8* (4), 3331-3336.
(68) Shemesh, N.; Adiri, T.; Cohen, Y. Probing microscopic architecture of opaque heterogeneous systems using double-pulsed-field-gradient NMR. *J. Am. Chem. Soc.* **2011**, *133* (15), 6028-6035.
(69) Shayegan, M.; Tahvildari, R.; Metera, K.; Kisley, L.; Michnick, S. W.; Leslie, S. R. Probing inhomogeneous diffusion in the microenvironments of phase-separated polymers under confinement. *J. Am. Chem. Soc.* **2019**, *141* (19), 7751-7757.
(70) Pastore, R.; Ciarlo, A.; Pesce, G.; Greco, F.; Sasso, A. Rapid Fickian yet non-Gaussian diffusion after subdiffusion. *Phys. Rev. Lett.* **2021**, *126* (15), 158003.

(71) Chechkin, A. V.; Seno, F.; Metzler, R.; Sokolov, I. M. Brownian yet non-Gaussian diffusion: from superstatistics to subordination of diffusing diffusivities. *Phys. Rev. X.* **2017**, *7* (2), 021002.
(72) Xue, C.; Zheng, X.; Chen, K.; Tian, Y.; Hu, G. Probing non-Gaussianity in confined diffusion of nanoparticles. *J. Phys. Chem, Lett.* **2016**, *7* (3), 514-519.
(73) Kwon, G.; Sung, B. J.; Yethiraj, A. Dynamics in crowded environments: is non-Gaussian Brownian diffusion normal? *J. Phys. Chem. B* **2014**, *118* (28), 8128-8134.
(74) Wang, B.; Kuo, J.; Bae, S. C.; Granick, S. When Brownian diffusion is not Gaussian. *Nat. Mater.* **2012**, *11* (6), 481-485.
(75) Goychuk, I.; Hänggi, P. Non-Markovian stochastic resonance. *Phys. Rev. Lett.* **2003**, *91* (7), 070601.
(76) Alonso, A. d. C.; Zaidi, T.; Grundke-Iqbal, I.; Iqbal, K. Role of abnormally phosphorylated tau in the breakdown of microtubules in Alzheimer disease. *Proc. Natl. Acad. Sci. U.S.A.* **1994**, *91* (12), 5562-5566.
(77) Gilley, J.; Ando, K.; Seereeram, A.; Rodríguez-Martín, T.; Pooler, A. M.; Sturdee, L.; Anderton, B. H.; Brion, J.-P.; Hanger, D. P.; Coleman, M. P. Mislocalization of neuronal tau in the absence of tangle pathology in phosphomutant tau knockin mice. *Neurobiol. Aging* **2016**, *39*, 1-18.
(78) Orr, M. E.; Sullivan, A. C.; Frost, B. A brief overview of tauopathy: causes, consequences, and therapeutic strategies. *Trends Pharmacol. Sci.* **2017**, *38* (7), 637-648.
(79) Rothman, J. S.; Kocsis, L.; Herzog, E.; Nusser, Z.; Silver, R. A. Physical determinants of vesicle mobility and supply at a central synapse. *Elife* **2016**, *5*, e15133.
(80) Longmire, M.; Choyke, P. L.; Kobayashi, H. Clearance properties of nano-sized particles and molecules as imaging agents: considerations and caveats. **2008**.
(81) Yang, D.; Dai, Y.; Liu, J.; Zhou, Y.; Chen, Y.; Li, C.; Lin, J. Ultra-small BaGdF5-based upconversion nanoparticles as drug carriers and multimodal imaging probes. *Biomaterials* **2014**, *35* (6), 2011-2023.
(82) Bastos, V.; Oskoei, P.; Andresen, E.; Saleh, M. I.; Rühle, B.; Resch-Genger, U.; Oliveira, H. Stability, dissolution, and cytotoxicity of NaYF4-upconversion nanoparticles with different coatings. *Sci. Rep.* **2022**, *12* (1), 3770.
(83) Park, M. V.; Neigh, A. M.; Vermeulen, J. P.; de la Fonteyne, L. J.; Verharen, H. W.; Briedé, J. J.; van Loveren, H.; de Jong, W. H. The effect of particle size on the cytotoxicity, inflammation, developmental toxicity and genotoxicity of silver nanoparticles. *Biomaterials* **2011**, *32* (36), 9810-9817.
(84) Mahata, M. K.; De, R.; Lee, K. T. Near-infrared-triggered upconverting nanoparticles for biomedicine applications. *Biomedicines* **2021**, *9* (7), 756.
(85) Wang, C.; Cheng, L.; Liu, Z. Upconversion nanoparticles for photodynamic therapy and other cancer therapeutics. *Theranostics* **2013**, *3* (5), 317.
(86) Punjabi, A.; Wu, X.; Tokatli-Apollon, A.; El-Rifai, M.; Lee, H.; Zhang, Y.; Wang, C.; Liu, Z.; Chan, E. M.; Duan, C. Amplifying the red-emission of upconverting nanoparticles for biocompatible clinically used prodrug-induced photodynamic therapy. *ACS nano* **2014**, *8* (10), 10621-10630.
(87) Mao, D.; Hu, F.; Yi, Z.; Kenry, N.; Xu, S.; Yan, S.; Luo, Z.; Wu, W.; Wang, Z.; Kong, D. AIEgen-coupled upconversion nanoparticles eradicate solid tumors through dual-mode ROS activation. *Sci. Adv.* **2020**, *6* (26), eabb2712.

(88) Wang, M.; Song, J.; Zhou, F.; Hoover, A. R.; Murray, C.; Zhou, B.; Wang, L.; Qu, J.; Chen, W. R. Nir-triggered phototherapy and immunotherapy via an antigen-capturing nanoplatform for metastatic cancer treatment. *Advanced Science* **2019**, *6* (10), 1802157.
(89) Han, S.; Hwang, B. W.; Jeon, E. Y.; Jung, D.; Lee, G. H.; Keum, D. H.; Kim, K. S.; Yun, S. H.; Cha, H. J.; Hahn, S. K. Upconversion nanoparticles/hyaluronate–rose bengal conjugate complex for noninvasive photochemical tissue bonding. *ACS nano* **2017**, *11* (10), 9979-9988.
(90) Park, S. J.; Song, S.; Yang, G.-S.; Kim, P. M.; Yoon, S.; Kim, J.-H.; Sung, J. The chemical fluctuation theorem governing gene expression. *Nat. Commun.* **2018**, *9* (1), 1-12.
(91) Poletayev, A. D.; Dawson, J. A.; Islam, M. S.; Lindenberg, A. M. Defect-driven anomalous transport in fast-ion conducting solid electrolytes. *Nat. Mater.* **2022**, *21* (9), 1066-1073.
(92) Zwanzig, R. Memory effects in irreversible thermodynamics. *Phys. Rev.* **1961**, *124* (4), 983.
(93) Mori, H. Transport, collective motion, and Brownian motion. *Prog. Theor. Phys.* **1965**, *33* (3), 423-455.
(94) Song, S.; Yang, G.-S.; Park, S. J.; Hong, S.; Kim, J.-H.; Sung, J. Frequency spectrum of chemical fluctuation: A probe of reaction mechanism and dynamics. *PLoS Comput. Biol.* **2019**, *15* (9), e1007356.
(95) Abate, J.; Valkó, P. P. Multi-precision Laplace transform inversion. *Int J Numer Methods Eng* **2004**, *60* (5), 979-993.

Figures and Tables

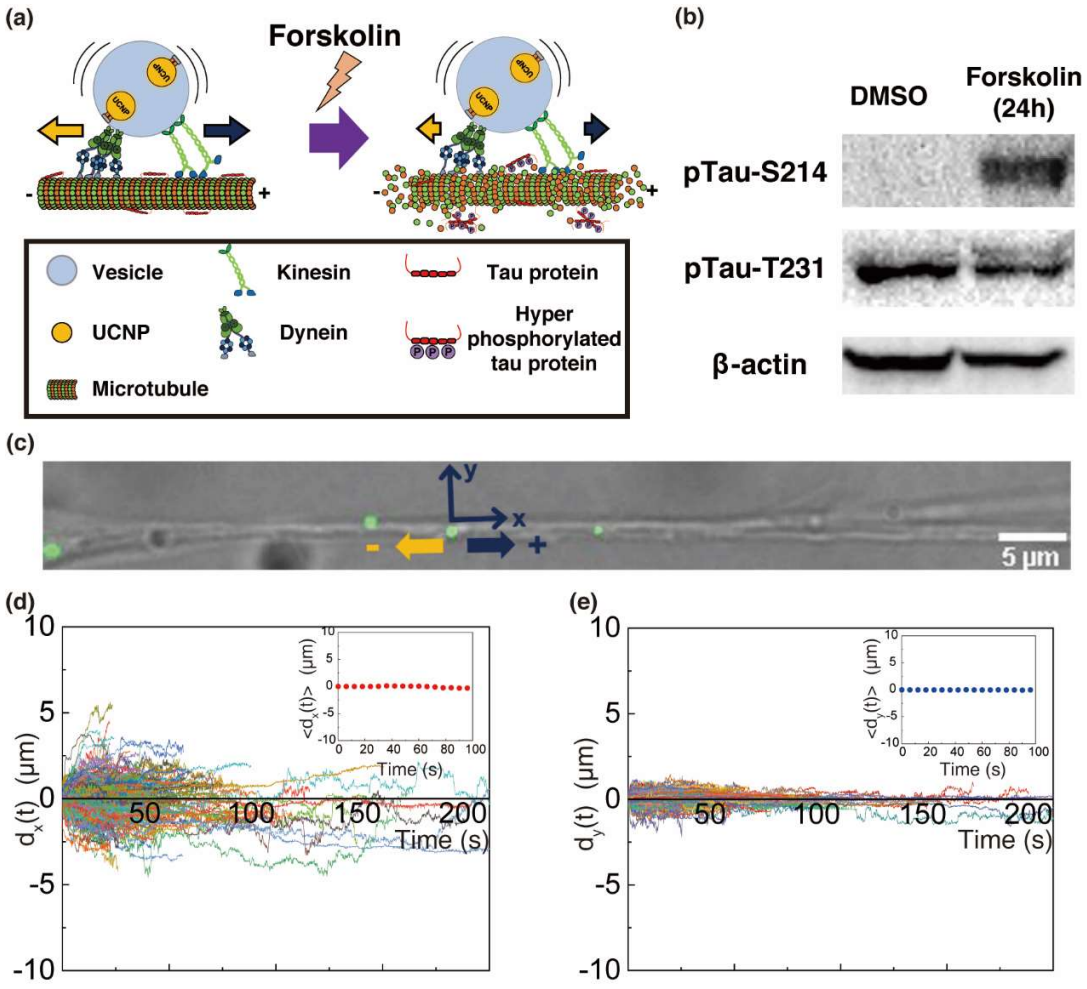

Figure 1. Trajectories of vesicle carried by motor protein multiplex on unstable microtubules in forskolin-treated cells. (a) Schematic representation of vesicle-motor protein multiplex (VMPM) on the microtubule in normal cells (left) and in forskolin-treated cells (right). Under forskolin treatment, microtubules are destabilized by hyperphosphorylation of tau proteins and ensuing tau detachment from the microtubules. Both kinesins and dyneins simultaneously carry and transport a vesicle along the microtubules. Vesicle-encapsulated upconverting nanoparticles

(UCNP) are employed to track vesicle motion in our cell systems. (b) Western blotting image after forskolin treatment (20 μM for 24 hours) in SH-SY5Y cells. Tau-hyperphosphorylation at SER-214 site is induced selectively by forskolin treatment (see Figure S2). (c) A snapshot of vesicle motion in live SH-SY5Y cells. The x-axis and y-axis directions designate the microtubule direction and microtubule-orthogonal direction, respectively. (d and e) Trajectories of VMPMs in the cells under hyperphosphorylation conditions. (insets) the mean displacement of VMPMs. In the hyperphosphorylated cells, trajectories of VMPMs have far different shapes from trajectories of VMPMs in normal cells (see Figure S4). The average motion of VMPMs is not biased in any direction.

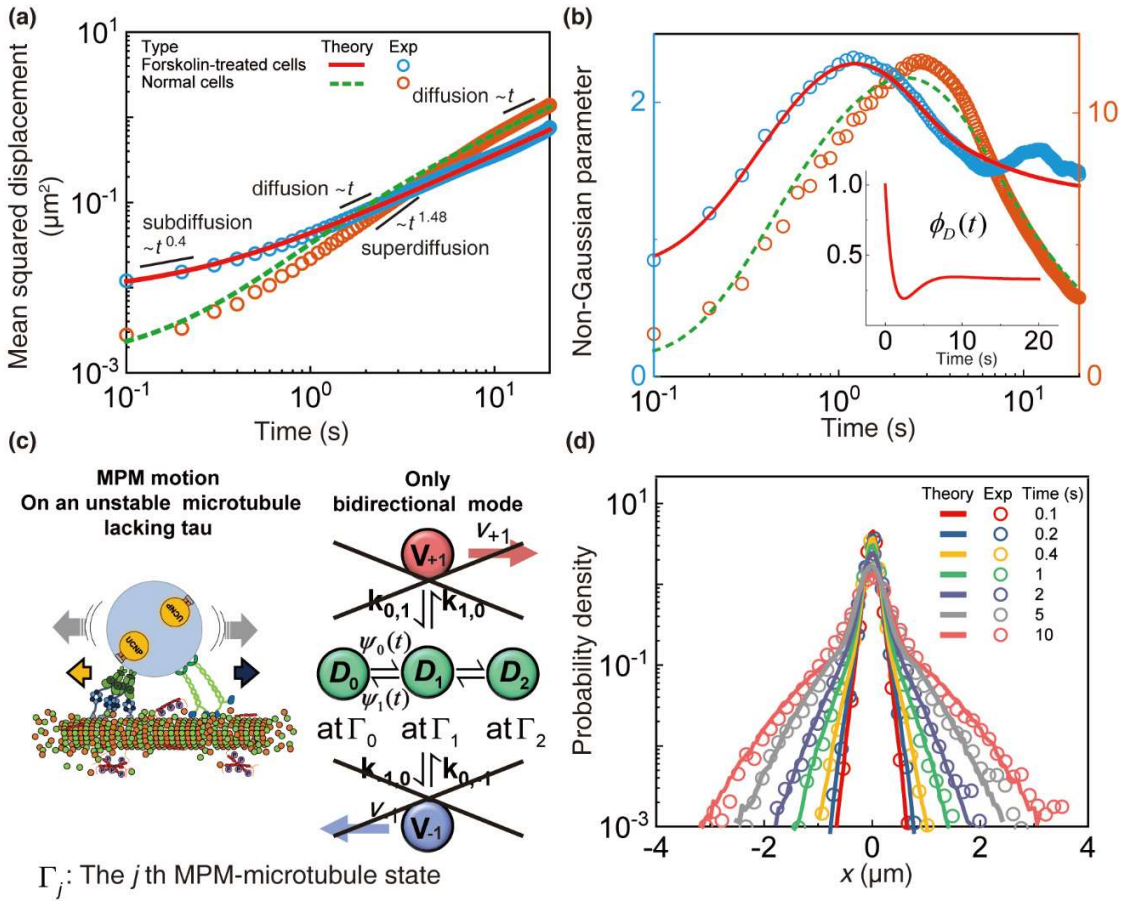

Figure 2. Mean square displacement, Non-Gaussian parameter, and Distribution of the vesicle motor protein multiplex's displacement along the microtubule. (a and b) The mean square displacement (MSD) and the non-Gaussian parameter (NGP) of VMPM motion along the microtubule: (blue circles) experiment results of the forskolin-treated cells (red line) theoretical result of eq 1 (see also Material and Methods). (orange circles) experiment results of the normal cells (green dashed line) theoretical result of the multimode MPM model (see Supplementary Method 2 in ref.[17]). In forskolin-treated cells, the MSD time-profile of VMPMs exhibits the direct transition from the initial sub-diffusion to ultimate diffusion without transient super-diffusion that emerges in the MSD time-profile in normal cells; at short times, liberational motion of a vesicle

bound to the MPM makes the dominant contribution to the MSD of the VMPM and at long times, diffusive motion of the MPM makes the dominant contribution to the MSD, i.e., $\langle d_x^2 \rangle \cong 2\langle D_\Gamma \rangle t$. (inset of B), The normalized time correlation function, $\phi_D(t)\left[\equiv \langle \delta D_\Gamma(t)\delta D_\Gamma(0)\rangle / \langle \delta D_\Gamma^2 \rangle\right]$, of diffusion coefficient fluctuation of the MPM, extracted from the MSD and NGP data using eq 2 without assuming a particular model. Using the time-profile of $\phi_D(t)$, we construct the explicit model of the MPM motility fluctuation, shown in (c). In (b), the left-y axis and right y-axis represent the NGP value in the forskolin-treated cells and the NGP value in the normal cells, respectively. (c) Schematic representation of the MPM motion on an unstable microtubule lacking tau in the forskolin-treated cells. Unidirectional motion of the MPM is suppressed. MPMs only bidirectional random motion with a partially dynamic motility fluctuation. Our model of the MPM motion with motility fluctuation is schematically represented. D_i designates the effective diffusion coefficient of the MPM in state Γ_i. A unified, quantitative explanation of our experimental results for the MSD and NGP time-profile is achieved when the waiting time distribution, $\psi_i(t) \quad i \in \{0,1\}$ of State Γ_0 or State Γ_1, is modeled by a gamma distribution (see Methods). (d) The VMPM displacement distribution in forskolin-treated cells: (circles) experiment results, (lines) theoretical predictions by our model optimized against the MSD and NGP data of VMPM motion in forskolin-treated cells.

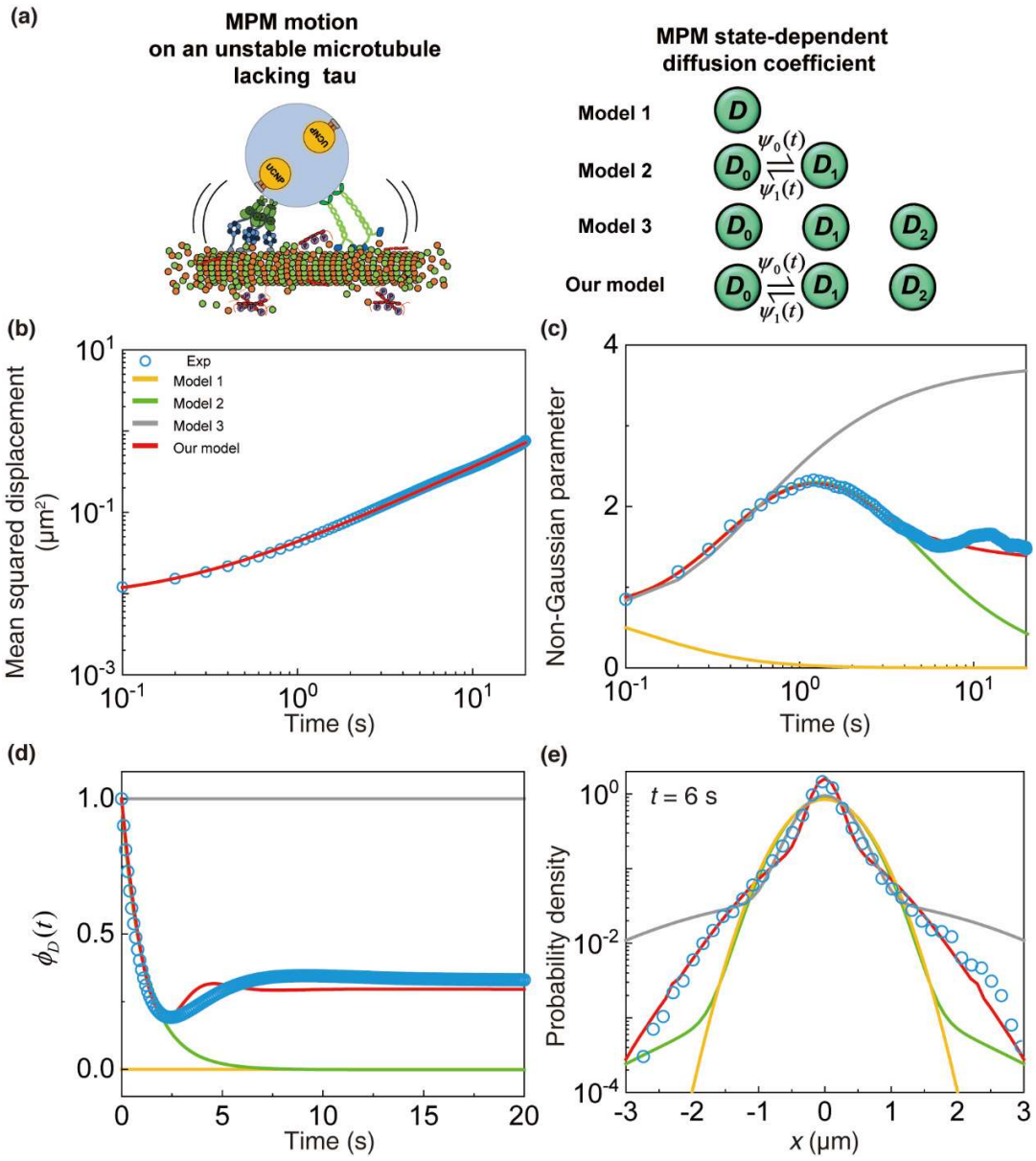

Figure 3. The MPM motility fluctuation dependent NGP time-profiles and the displace distribution of VMPMs. (a) Various models of the MPM state dynamics. At the MPM state Γ_i, the MPM undergo diffusive random motion with the MPM state-dependent diffusion coefficient, D_i. $\psi_i(t)$ denotes the lifetime distribution of the MPM state Γ_i, modeled as a gamma distribution. See Table 2 for the parameter values used in the theoretical calculation for Model 1-3. For our

model, the parameter values are listed in Table 1. (b and c) Time-profiles of the MSD and NGP of the VMPM. Theoretical results are calculated by eq 1 for all models. (d) Time correlation function of the diffusion coefficient fluctuation calculated for each model. For model 1, $\delta D = \phi_D(t) = 0$. For Model 2, the TCF is given by eq 4 with $p_2 = 0$. The values of other parameters are given in Table 2. For Model 3, $\phi_D(t) = 1$ because $\langle \delta D_{\mathbf{\Gamma}}(t) \delta D_{\mathbf{\Gamma}}(0) \rangle = \langle \delta D_{\mathbf{\Gamma}}^2 \rangle$ at all time *t*. The TCF of Model 3 is given by eq 4 with $G(\Gamma_i, t \mid \Gamma_j)$ replaced by $G(\Gamma_i, t \mid \Gamma_j) = \delta_{ij}$ with δ_{ij} denoting the Kronecker delta. The TCF of our model is given by eq 4. (e) The VMPM displacement distribution (VDD) at 6.0 sec. Theoretical results are calculated by numerical inversion of eq 16[95], where the expressions of $\hat{\tilde{P}}(k,s)$ are given in Table 3 for Model 1, 2, and 3. For our model, $\hat{\tilde{P}}(k,s)$ is given in eq 14. For all models, $\tilde{f}(k)$ in eq 16 is given by eq 13. Model 1, 2, and 3 cannot explain our experimental results of the non-Gaussian parameter and the VDD regardless of the parameter values.

Table 1. Optimized values of the adjustable parameters of the vesicle-motor protein multiplex model shown in Figure 2c.

Adjustable parameters	Values
D_0	8.95×10^{-3} μm^2/s
D_1	1.18×10^{-1} μm^2/s
D_2	2.12×10^{-3} μm^2/s
p_2	0.626
$\langle t_0\rangle$	2.85 s
$\langle \delta t_0^2\rangle / \langle t_0\rangle^2$	0.14
$\langle t_1\rangle$	1.34 s
$\langle \delta t_1^2\rangle / \langle t_1\rangle^2$	0.74

D_0, D_1, and D_2 designate the effective diffusion coefficient characterizing the bidirectional motion of the MPM at states, Γ_0, Γ_1, and Γ_2, respectively. p_2 denotes the probability that a vesicle is in State Γ_2. The probabilities, p_0 and p_1, of State Γ_0 and State Γ_1 are related to p_2 by $p_0 = (1-p_2)\langle t_0\rangle / \left(\langle t_0\rangle + \langle t_1\rangle\right) \cong 0.254$ and $p_1 = (1-p_2)\langle t_1\rangle / \left(\langle t_0\rangle + \langle t_1\rangle\right) \cong 0.120$, where $\langle t_i\rangle$ denotes the mean lifetime of State Γ_i. $\langle \delta t_i^2\rangle / \langle t_i\rangle^2$ denotes the relative variance of the lifetime distribution $\psi_i(t)$ of State Γ_i, which is modeled by a gamma distribution, i.e., $\psi_i(t) = b_i^{-a_i} t^{a_i-1} e^{-t/b_i} / \Gamma(a_i),\ i \in \{0,1\}$ with $\langle t_i\rangle = a_i b_i$ and $\langle \delta t_i^2\rangle / \langle t_i\rangle^2 = a_i^{-1}$. The values of these parameters are extracted from the time-profiles of the mean square displacement and the non-

Gaussian parameter of the vesicle-motor protein multiplex motion in forskolin-treated cells, shown in Figures 2a and b.

Table 2. Parameter values used in the calculation for Model 1-3 shown in Figure 3.

Adjustable parameters	Model 1	Model 2	Model 3
D	$0.0177\mu m^2/s$	-	-
D_0	-	$9.89\times10^{-1}\mu m^2/s$	$7.98\times10^{-1}\mu m^2/s$
D_1	-	$1.63\times10^{-2}\mu m^2/s$	$2.85\times10^{-1}\mu m^2/s$
D_2	-	-	$9.77\times10^{-3}\mu m^2/s$
p_0	-	1.46×10^{-3}	8.99×10^{-3}
p_1	-	9.98×10^{-1}	1.76×10^{-1}
p_2	-	-	8.15×10^{-1}
$\langle t_0\rangle$	-	1.23s	-
$\langle \delta t_0^2\rangle/\langle t_0\rangle^2$	-	8.91×10^{-1}	-
$\langle t_1\rangle$	-	8.44×10^{2}s	-
$\langle \delta t_1^2\rangle/\langle t_1\rangle^2$	-	3.35×10^{-2}	-

In Model 1, the MPM has a single state. D denotes the diffusion coefficient characterizing the bidirectional motion of the MPM at the state. In Model 2, the MPM has two different states, Γ_0 and Γ_1. D_j denotes the diffusion coefficient of the MPM at state Γ_j. The lifetime distribution $\psi_j(t)$ of MPM state Γ_j is modeled as a gamma distribution as in our model (see Table 1 caption). $\langle t_j\rangle$ and $\langle \delta t_j^2\rangle$ denote the mean and variance of the lifetime of the MPM state Γ_j. p_j denotes the equilibrium probability of MPM state Γ_j. p_0 and p_1 are given by $p_0=\langle t_0\rangle/\left(\langle t_0\rangle+\langle t_1\rangle\right)$ and

$p_1 = 1 - p_0$. In Model 3, the MPM has three different states, Γ_0, Γ_1, and Γ_2, and there is no transition among the three states. Model 1, 2, and 3 cannot explain our experimental results of the NGP time-profile and the VMPM displacement distribution regardless of parameter values.

Table 3. Analytic expression of $\hat{\tilde{P}}(k,s)$ for Model 1,2, and 3 shown in Figure 3.

Model 1	$\frac{1}{s+Dk^2}$
Model 2	$\frac{p_0}{s_0}+\frac{p_1}{s_1}-\frac{\left[1-\hat{\psi}_0(s_0)\right]\left[1-\hat{\psi}_1(s_1)\right]}{(\langle t_0\rangle+\langle t_1\rangle)\left[1-\hat{\psi}_0(s_0)\hat{\psi}_1(s_1)\right]}\left(\frac{1}{s_0}-\frac{1}{s_1}\right)^2$
Model 3	$\frac{p_0}{s_0}+\frac{p_1}{s_1}+\frac{p_2}{s_2}$

$\hat{\tilde{P}}(k,s)$ designates the Fourier-Laplace transform of the probability distribution of the motor-protein-multiplex (MPM) displacement, i.e., $\hat{\tilde{P}}(k,s)=\int_{-\infty}^{\infty}dR_x\exp(ikR_x)\int_0^{\infty}ds\exp(-st)P(R_x,t)$. D, D_j, $\langle t_0\rangle$ and $\langle t_1\rangle$ have the same meaning as in Table 2. s_j denotes $s+D_jk^2$ with s being the Laplace variable. $\hat{\psi}_j(s)$ denotes the Laplace transform of the lifetime distribution $\psi_j(t)$ of the MPM state Γ_j, i.e., $\hat{\psi}_j(s)=\int_0^{\infty}dte^{-st}\psi_j(t)$. $\psi_j(t)$ is modeled as a gamma distribution (see caption of Table 1).

For Table of Contents Only